Available online at www.sciencedirect.com

SciVerse ScienceDirect

journal homepage: www.elsevier.com/locate/he

Catalytic partial oxidation of methane rich mixtures in non-adiabatic monolith reactors

J.E.P. Navalho [a], I. Frenzel [b], A. Loukou [b], J.M.C. Pereira [a,*], D. Trimis [b], J.C.F. Pereira [a]

[a] Universidade Técnica de Lisboa, Instituto Superior Técnico, Mechanical Engineering Department, LASEF, Av. Rovisco Pais 1, 1049-001 Lisbon, Portugal

[b] Technische Universität Bergakademie Freiberg, Institute of Thermal Engineering, Chair of Gas and Heat Technology, Gustav-Zeuner-Str. 7, 09596 Freiberg, Germany

ARTICLE INFO

Article history:
Received 30 October 2012
Received in revised form
21 February 2013
Accepted 28 February 2013
Available online 24 April 2013

Keywords:
Reforming
Catalytic partial oxidation
Non-adiabatic reactor
Radiative heat losses
Methane
Synthesis gas

ABSTRACT

In this work the partial oxidation of hydrocarbons on a rhodium-based catalyst is studied experimentally and numerically. A unidimensional heterogeneous mathematical model for catalytic partial oxidation of hydrocarbons is applied to adiabatic and non-adiabatic honeycomb monolith reactors. The model is validated for the non-adiabatic case with good agreement against experimental measurements of temperature and species concentrations for three fuel compositions over a wide range of operating conditions.

The influence of radiative heat losses on the non-adiabatic reactor performance is numerically investigated under varying operating conditions: fuel flow rate, air to fuel equivalence ratio and fuel composition. The radiative heat losses change the heat release relatively to the adiabatic configuration and a slightly more exothermic reaction pathway is observed. This higher chemical heat release points out a lower importance of endothermic reforming reactions in the overall chemical scheme justifying the lower outlet fuel conversion registered. It is also observed during non-adiabatic operation that the H_2 selectivity can present higher values than in adiabatic conditions.

The potential of the non-adiabatic reactor configuration to improve catalyst thermal stability is confirmed since a significant decrease of surface hot spots in relation to adiabatic operation may occur.

1. Introduction

Catalytic partial oxidation (CPOx) of hydrocarbons has received growing attention during the last 20 years. A renewed interest on this process arose after Schmidt and co-workers [1–4] reported high values of methane conversion and synthesis gas selectivity in autothermal and millisecond contact time monolith reactors coated with noble metal catalysts (Rh and Pt). The catalytic partial oxidation reaction of hydrocarbons (expression (1)) is globally exothermic ($\Delta H_R^\circ < 0$) and its practical implementation reveals several advantages over other well-established reforming technologies such as the highly endothermic steam reforming technology since it does not require external heat sources, it can be performed in small, simple and compact reactors with low heat capacity and good heat transfer properties, allowing a fast transient response to changes in operating conditions and shorter start-up times [5]. These features enable the catalytic partial

* Corresponding author.
E-mail address: jose.chaves@ist.utl.pt (J.M.C. Pereira).

0360-3199/$ – see front matter
http://dx.doi.org/10.1016/j.ijhydene.2013.02.141

Nomenclature

A	area; total monolith frontal area (expression (21)), m^2
C_k	molar concentration of species k, mol m^{-3}
C_p	specific heat capacity at constant pressure, J kg^{-1} K^{-1}
D	diffusion coefficient, m^2 s^{-1}
H_k	molar enthalpy of species k, J mol^{-1}
KK	total number of species
$K_{mat,k}$	interphase mass transport coefficient, m s^{-1}
L	length, m
LHV	low heating value, J mol^{-1}
N_R	total number of reactions
N_s	total number of surface zones
P	total pressure, Pa
P_k	partial pressure of species k, Pa
Pe	Péclet number
R	universal gas constant, J mol^{-1} K^{-1}
S_{CO}	integral carbon monoxide selectivity
S_{H_2}	integral hydrogen selectivity
T	temperature, K
W	molecular weight, kg mol^{-1}
X_{CH_4}	integral methane conversion
Y_k	mass fraction of species k
$\dot{V}_{fuel}$	volumetric fuel flow rate, m^3 s^{-1}
$\dot{n}$	molar flux, mol s^{-1}
$\dot{q}_{chem.}$	chemical heat release, evaluated with the denominator of expression (21), W m^{-2}
$\dot{q}_{net}$	net heat release, W m^{-2}
$\dot{q}_{rad_{loss}}$	radiative heat loss, W m^{-2}
a_V	specific surface area, m^{-1}
d_h	hydraulic diameter of monolith channels, m
h	interphase heat transport coefficient, W m^{-2} K^{-1}
k	thermal conductivity, W m^{-1} K^{-1}
q''_{Rad}	net radiative heat flux, W m^{-2}
q_R	rate-of-progress variable of reaction R, mol $kg_{cat.}^{-1}$ s^{-1}
t	time, s
u	axial mean flow velocity, m s^{-1}
x	axial reactor coordinate, m

Greek letters

$\delta_{cat.}$	washcoat thickness, m
$\dot{\omega}$	molecular production/consumption rate, mol $m_{cat.}^{-3}$ s^{-1}
ε	porosity
ε_i	emissivity of surface zone i
$\eta_{ref.}$	integral reforming efficiency
η_R	generalized effectiveness factor of reaction R
λ	air to fuel equivalence ratio
$\nu_{k,R}$	stoichiometric coefficient of species k in reaction R
Ω	relative radiative heat losses
φ	generalized Thiele modulus
ρ	density, kg m^{-3}
σ	Stefan–Boltzmann constant, W m^{-2} K^{-4}
ξ	catalytic volumetric fraction

Subscripts

$cat.$	catalyst
ef	effective
g	gas phase; gas species
in	inlet
k	species k
out	outlet
s	solid phase
s_i	surface zone i
w	wall species; washcoat

Superscirpts

eq	chemical equilibrium conditions
S	external washcoat surface conditions

oxidation for small-scale stationary or on-board applications namely to feed fuel cells for electric power generation purposes [6,7].

$$C_xH_y + \frac{x}{2}O_2 \rightarrow xCO + \frac{y}{2}H_2 \quad (1)$$

Noble metal catalysts, namely Rh and Pt, have shown great activity for catalytic partial oxidation of hydrocarbons and low tendency to deactivate due to coke deposition [8]. For these reasons many of the mechanistic works available in the literature about methane CPOx are devoted to noble metal catalysts. Several reaction mechanisms were proposed in literature for methane CPOx over Rh catalysts ranging from detailed multi-step surface mechanisms [3,9–11] to global surface mechanisms expressed by Langmuir–Hinshelwood rate equations [12–14]. Recently, an interest on CPOx of higher hydrocarbons (logistic fuels) has been also visible in literature [15–18] mainly motivated by mobile applications [7]. Propane CPOx on Rh-based catalyst has also received attention [19] as well as butane [20,21].

The knowledge of the intrinsic kinetics is a key issue in numerical modeling endeavors. With a reliable reaction mechanism as well as by accounting for proper heat and mass transport mechanisms the numerical models can support reactor improvements.

One dimensional mathematical models have been broadly used in literature to capture the reactor performance in an expedite way [13,22–30]. Dalle Nogare et al. [26] applied a plug flow model and a heterogeneous model, both considering detailed methane CPOx chemistry [9], and concluded that the former was not adequate to accurately predict species profiles in the first region of the catalyst while the heterogeneous model gave satisfactory results in the whole range of the catalyst. Maestri et al. [13] applied a heterogeneous dynamic model, considering radiation in solid phase through an effective conductivity and employing global methane CPOx chemistry, to analyze the performance of spheres, in a packed bed reactor, foam and honeycomb monoliths with emphasis on the role of external transport properties on steady-state and start-up regimes. Tavazzi et al. [25] concluded for a packed bed reactor that high feed flow rates and low preheating temperatures contribute to reduce the relative heat losses from the reactor, improving its adiabaticity. For honeycomb monoliths the influence of the flow rate on reactor

performance was explored experimentally by Liu et al. [31] and also numerically by Beretta et al. [28].

The influence of the fuel composition on methane CPOx, namely through the addition of other chemical species (N_2, CO_2 or H_2O) to the inlet feed stream has also been analyzed [22,30,32–34]. In particular, Donazzi et al. [34] demonstrated experimentally and numerically that diluting methane/air mixtures with a constant C/O ratio and total flow rate with N_2 or CO_2 the gas temperatures and fuel conversion decrease whereas the integral H_2/CO ratio increased for N_2 and decreased for CO_2 dilution.

The application of a washcoat layer on the catalyst substrate is a common practice in heterogeneous catalysis. Its main purpose is to increase the catalytic surface area through the deposition of catalyst metals onto surfaces of a highly porous material. However, mass and heat transfer resistances along the washcoat thickness will always appear in some extent but the washcoat application is largely accepted as more profitable [35,36]. In modeling studies, the effect of diffusional resistances along the washcoat layer has been treated by a simplified approach, using isothermal effectiveness factors neglecting the usually less important thermal gradients [35].

Radiative heat transfer can play an important role on the overall heat transfer phenomena due to the high temperature gradients that arise in some sections of a catalytic monolith reactor [37–40]. The main effect addressed to thermal radiation is to smooth temperature gradients redistributing the energy released by chemical reactions along the catalyst bed. In the majority of 1D CPOx heterogeneous modeling studies, radiative heat transfer in the solid phase has been accounted for through an effective heat conductivity corrected with a radiative contribution. For instance, concerning honeycomb monoliths Lee and Aris radiative correlation [37] has been extensively applied. In fact, the diffusion approximation of radiative heat transfer significantly reduces the complexity of the underlying heat transfer mechanism but it should be noted that near the boundaries of a non-adiabatic reactor, where radiative heat losses to surroundings are expected, this approach is not well suitable [41].

Radiative heat losses from the interior of CPOx reactors, to the authors knowledge, have received little attention in literature, mostly due to the axial radiative insulation provided by the application of inert heat shields that surround the catalytic structure. However, even with the application of heat shields a perfect insulation is not guaranteed and most of modeling studies only account for radiative losses on boundary conditions [25,28,30].

The absence of appropriate catalyst axial insulation can be a requirement for CPOx reactor integration on a specific application. In this case, besides radiative heat losses from the blank inlet monolith end (accounted for on boundary conditions) radiant heat fluxes are also expected to occur from the interior catalyst bed which should be taken into account through a proper radiative method on the energy balances of the mathematical model. The experimental work conducted by Seyed-Reihani and Jackson [20] studied the influence of operating conditions on n-butane partial oxidation over $Rh/\gamma-Al_2O_3$ washcoated $\alpha-Al_2O_3$ foams in insulated and non-insulated reactor configurations. In their work heat losses were attributed indistinctly to conduction and radiation from the reactor and were calculated through an enthalpy balance with measured inlet and outlet species and temperature data. Significant differences on reactor performance were concluded.

For other applications of catalytic combustion, using honeycomb monoliths without heat shields, radiative heat losses have been a topic of debate. For example, Boehman [38] studied the role of radiative heat transfer in the thermal behavior of a honeycomb monolith applied in catalytic combustion of methane with the net radiation method and concluded that radiation exerts an important function at the ends of the monolith but the surface emissivity did not influence significantly the reactor behavior. Mazumder and Grimm [42] concluded during methane combustion on Pt catalysts that the surface emissivity has an important effect in transient and steady-state regimes, in disagreement with Boehman [38] and the gas phase mixture has a negligible radiative role comparing to surface-to-surface radiant heat exchange.

A well-known serious disadvantage during catalytic partial oxidation operation is the occurrence of surface hot spots which can lead to an unhealthy catalyst thermal behavior as the time-on-stream increases since high catalyst temperatures can trigger thermal deactivation mechanisms (sintering of metal particles or phase transformations of the catalyst carrier). To extend the catalyst life-time, severe operating conditions (high fuel flow rates and high preheating temperatures) should be avoided [28]. An even worse performance regarding hot spot formation is expected during CPOx of higher hydrocarbons due to the higher reaction enthalpies associated. Several strategies have been proposed to overcome this limitation [22,30,43]. In particular, the non-adiabatic reactor operation was recently analyzed as an effective way to decrease hot spot formation since lower surface temperatures are achieved due to the radiation dispersion from the catalyst bed to the surroundings [44].

The objective of this paper is firstly to validate the numerical model with experimental measurements of a non-adiabatic reactor and secondly to investigate the influence of radiative heat losses from the non-adiabatic reactor on its performance, for several values of fuel flow rate and air to fuel equivalence ratio, considering pure methane as the reference fuel. The effect of fuel composition is also assessed under comparable operating conditions for three fuel samples surrogate of natural gas: pure methane (denoted as G20 fuel), 85% CH_4 + 15% N_2 (G231 fuel) and 87% CH_4 + 13% C_3H_8 (G21 fuel). New experimental results for catalytic partial oxidation within a non-adiabatic honeycomb monolith coated with a Rh-based catalyst are presented for the three fuel samples. Integral product distribution and temperature profiles measured along the catalyst length allowed the validation of a 1D heterogeneous mathematical model. The model accounts for proper surface chemistry, internal diffusional limitations along the washcoat layer and for radiative heat transport along the catalyst bed.

The next section describes the experimental setup and method. Section 3 is concerned with a detailed description of the models used. Section 4 starts with the validation of the model predictions for the three fuel compositions against

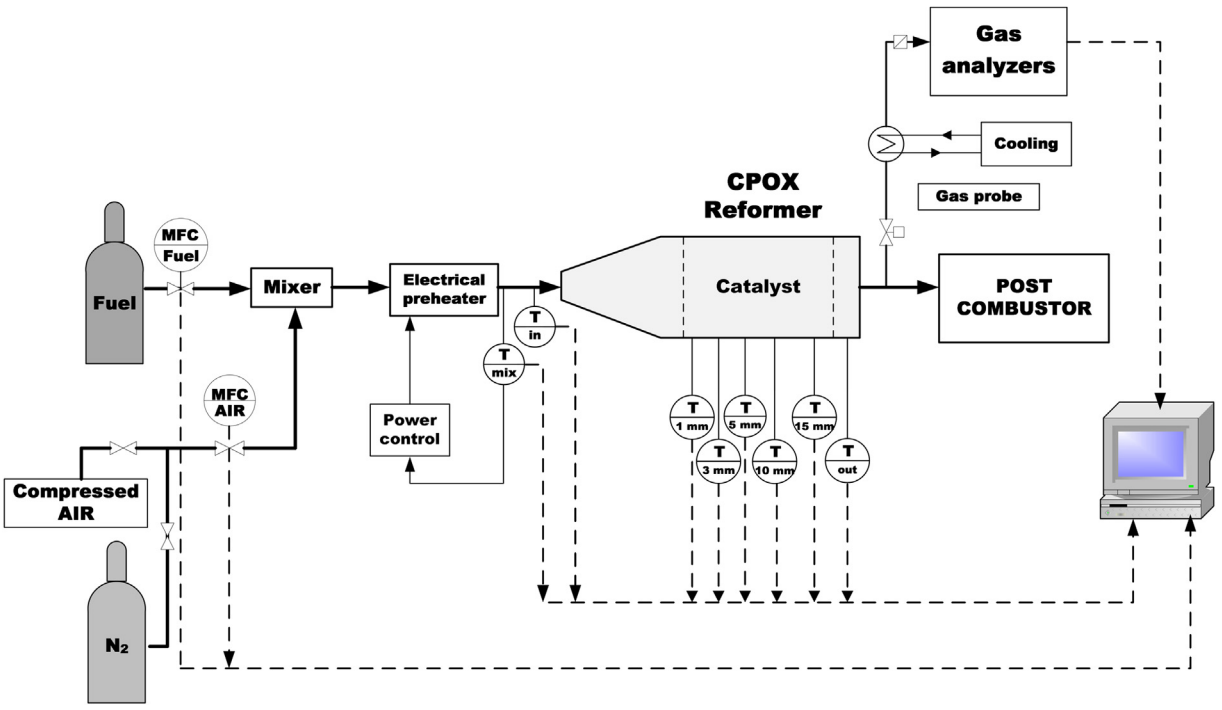

Fig. 1 – Flowsheet of the experimental setup.

experimental measurements. This is followed by the presentation of the results concerning the influence of radiative heat losses. The paper ends with summary conclusions.

2. Experimental

2.1. *Experimental setup*

A schematic image of the setup used for the conduction of experimental investigations is shown in Fig. 1. The setup is composed by the CPOx reactor and the control and measurement instrumentation.

The reactor consists of a conical section, where the premixed fuel/air mixture enters the reformer and a cylindrical part, where the catalyst is placed. The catalyst is fixed in the cylindrical metallic tube by wrapping it in a thin mat stripe. An inert front heat shield was not applied upstream the catalytic monolith and therefore a non-adiabatic reactor operation is expected. The metallic housing of the reactor is made out of high-temperature resistant stainless steel with a maximum outer diameter of 48.2 mm and a total length of 170 mm. The catalytic monolith herein employed is composed by a 600/3.5 cordierite honeycomb monolith (substrate) and on the walls a washcoat layer was deposited. The catalyst composition was assumed to be 4 wt.% $Rh/\alpha - Al_2O_3$ during the numerical analysis by employing a kinetic scheme developed for this catalyst formulation without any kinetic scaling procedure. Geometrical and thermo-physical properties of the catalytic monolith are presented in Tables 1 and 2, respectively.

The two gas streams were supplied to the system via thermal mass flow controllers. Pure methane 2.5 (G20, > 99.5%) and a mixture of 87% methane and 13% propane (G21, > 95%) from high pressure bottles were used as fuel. For preparation of G231 (85% methane and 15% nitrogen) pure nitrogen (99.8%) from high pressure bottles was supplied via thermal mass flow controllers as well and was mixed with methane to get the desired mixture.

Electrical preheating was used to increase the temperature of the fuel/air mixture at the inlet of the reformer up to 400 °C. A K-type thermocouple (with Inconel protection sheath of 1.5 mm in diameter) was used for monitoring and controlling

Table 1 – Geometrical properties of the honeycomb monolith catalyst after washcoat application.

Monolith diameter [cm]	3.70
Monolith length [cm]	2.00
Cell density [cpsi]	600
Cell shape [–]	Square
Bed porosity [%]	70.00
Specific surface area [cm^{-1}]	32.27
Cell hydraulic diameter [cm]	0.087
Washcoat thickness [μm]	40.00

Table 2 – Thermo-physical properties of the honeycomb monolith catalyst.

Solid conductivity [$W\,m^{-1}\,K^{-1}$]	3.00
Washcoat density [$g\,cm^{-3}$]	1.50
Surface emissivities [–]	
Inlet/outlet manifold surfaces	0.15
Washcoat surfaces	0.45
Blank monolith ends	0.50

at the same time the temperature of the fuel/air mixture upstream the reforming section. Another thermocouple (N-type, with Inconel protection sheath of 1.5 mm in diameter) was placed just upstream the catalytic monolith inlet section.

The axial temperature distribution within the catalytic monolith was measured with K-type thermocouples (with Inconel protection sheath of 0.5 mm in diameter). Each of the five thermocouples was placed inside different channels of the monolith 1, 3, 5, 10 and 15 mm in axial direction. An N-type thermocouple (with Inconel protection sheath of 1.5 mm in diameter) was placed 5 mm downstream the catalyst with the tip reaching the center axis of the reactor to measure the outlet temperature of the produced reformate. All the thermocouples were connected to the data acquisition system through a data acquisition board and the obtained values were recorded with a sampling frequency of 1 Hz.

Exhaust samples were collected via a stainless-steel, air-cooled probe. The probed sample was sent to calibrated gas analyzers (Table 3) and was on-line analyzed for H_2, CO, CO_2 and CH_4. Condensed phases were removed upstream the gas analyzers via a teflon filter and a condensate trap. Therefore, the amount of H_2O in the reformate was recalculated from measurements of the rest of the major species and the mass balance of the process. The uncertainties on the measurements of the species in dry condition were estimated on the basis of the accuracy and repeatability characteristics of the gas analyzers and are shown in Table 3. The remaining major part of the explosive and toxic product gas was incinerated in a post-combustor to primarily decrease the carbon monoxide content.

2.2. *Experimental method*

The same experimental procedure was followed for operating the reformer with the three different fuels. During the start-up, an air stream of 30 NL/min was electrically preheated so as to warm-up the reactor and to reach a temperature of minimum 270 °C within the monolith. After reaching this temperature a fuel flow of 2 NL/min and an air to fuel equivalence ratio of 0.34 were applied to ignite the reformer. Afterward, the operating conditions, in terms of fuel flow rate and air to fuel equivalence ratio were set to the test points, keeping stable the preheating temperature of the unreacted gas mixture. During transition from one test point to another, the reformer would run until completely stationary operation could be assured (ca. 15 min), before any measurement was taken for evaluation.

The air to fuel equivalence ratio (λ) is defined as the ratio between the actual and the stoichiometric air to fuel ratios. For a methane/air mixture the stoichiometric air to fuel ratio is based on the stoichiometry of methane total oxidation reaction. In terms of inlet O_2 and CH_4 molar fluxes the air to fuel equivalence ratio is given as expression (2) shows.

$$\lambda = \frac{\dot{n}_{O_2}}{2\dot{n}_{CH_4}} \tag{2}$$

The operating behavior of the reformer was scanned varying the air to fuel equivalence ratio from $\lambda = 0.29$ up to $\lambda = 0.33$ in steps of 0.02 and the fuel flow in the range of 2 NL/min up to 8 NL/min. An important consideration during testing has been the stability of the catalyst and consequently the highest temperatures occurring within the monolith during operation. In the case of the utilized catalysts, limit temperatures for long-term operation are considered to be at around 1000 °C. Thus, the investigations have been focused at identifying operating conditions which will ensure such temperature levels and efficient syngas production at the same time. To assure a stable operating regime without loss of catalyst activity due to thermal deactivation mechanisms, during all experimental characterization, a standard experimental run was initially performed with pure methane and using a fresh catalyst. The same experiment was performed periodically in order to detect discrepancies between measured data and the reference one. During the collection of all experimental data herein presented no signs of catalyst deactivation were observed.

For all the tested points and the three different fuels temperature profiles within the reaction zone and exhaust gas compositions were recorded. The uncertainty of the air to fuel equivalence ratio has been estimated on the basis of the mass flow controllers' accuracy which is ±1% of the full scale flow for all applied streams. The resulting error on λ depends on the fuel flow and is $\Delta\lambda < \pm 0.016$ for all applied conditions.

3. Modeling

3.1. *Governing equations*

Numerical results herein presented were performed with a 1D heterogeneous mathematical model using the so-called single channel approach. Being heterogeneous the model is able to predict thermal and species profiles for gas and solid phases along the axial dimension of the reactor.

3.1.1. *Gas phase balance equations*

The species mass and energy balance equations of gas phase read as:

Table 3 – Gas analyzers system with uncertainties in measurement of species.

Species	Detector	Measurement range [Vol.-%]	Uncertainty (combination of linearity deviation and repeatability) [±, Vol.-%]
H_2	Thermal Conductivity Detector (TCD)	0–25	0.156
CO_2	Infrared	0–20	0.025
CO	Spectroscopy	0–20	0.025
CH_4	(NDIR)	0–25	0.039

Table 4 – Kinetic scheme for catalytic partial oxidation of G20 and G231 fuels (R1 to R6) and for G21 fuel (R1 to R8).

$CH_4 + 2O_2 \rightarrow CO_2 + 2H_2O$	(R1)
$CH_4 + H_2O \rightleftarrows 3H_2 + CO$	(R2)
$CO + H_2O \rightarrow CO_2 + H_2$	(R3)
$CO_2 + H_2 \rightarrow CO + H_2O$	(R4)
$H_2 + \frac{1}{2}O_2 \rightarrow H_2O$	(R5)
$CO + \frac{1}{2}O_2 \rightarrow CO_2$	(R6)
$C_3H_8 + 5O_2 \rightarrow 3CO_2 + 4H_2O$	(R7)
$C_3H_8 + 3H_2O \rightleftarrows 7H_2 + 3CO$	(R8)

Mass balance equation

$$\varepsilon\rho_g\frac{\partial Y_{k,g}}{\partial t} + \varepsilon\rho_g u\frac{\partial Y_{k,g}}{\partial x} - \frac{\partial}{\partial x}\left(\varepsilon\rho_g D_{k,g}\frac{\partial Y_{k,g}}{\partial x}\right) + a_V\rho_g K_{mat,k}\left(Y_{k,g} - Y_{k,w}\right) = 0 \quad (3)$$

Energy balance equation

$$\varepsilon\rho_g C_{p,g}\frac{\partial T_g}{\partial t} + \varepsilon\rho_g u C_{p,g}\frac{\partial T_g}{\partial x} - \frac{\partial}{\partial x}\left(\varepsilon k_g\frac{\partial T_g}{\partial x}\right) - \varepsilon\rho_g\sum_{k=1}^{KK_g} D_{k,g}C_{p,k}\frac{\partial Y_{k,g}}{\partial x}\frac{\partial T_g}{\partial x} + a_V h\left(T_g - T_s\right) = 0 \quad (4)$$

Thermal diffusion (Soret effect) is also included on molecular diffusion. The overall mass conservation is assured through the correction velocity formalism due to the non-conservative mixture-averaged formalism employed to evaluate the ordinary molecular diffusion coefficients [45,46]. Momentum balance was not considered in the model scheme since the pressure drop along the monolith length is typically negligible [5,28]. Following literature knowledge homogeneous gas phase reactions were also neglected, even for G21 fuel case due to the small propane content [9,43,47]. The reactive flow behaves as an ideal gas mixture and consequently it obeys to the ideal gas equation given by expression (5).

$$\rho_g = \frac{PW_g}{RT_g} \quad (5)$$

3.1.2. *Solid phase balance equations*

The species mass and energy balance equations of solid phase read as:

Mass balance equation

$$\varepsilon_w\xi\rho_g\frac{dY_{k,w}}{dt} - a_V\rho_g K_{mat,k}\left(Y_{k,g} - Y_{k,w}\right) - \xi\dot{\omega}_{k,w}W_k = 0 \quad (6)$$

Energy balance equation

$$(1-\varepsilon)\rho_s C_{p,s}\frac{\partial T_s}{\partial t} - \frac{\partial}{\partial x}\left(k_{s,ef}\frac{\partial T_s}{\partial x}\right) - a_V h\left(T_g - T_s\right) + \xi\sum_{k=1}^{KK_w}\dot{\omega}_{k,w}H_k + a_V q''_{Rad} = 0 \quad (7)$$

Solid and gas phases are coupled in terms of mass and energy balances through interphase transport of mass and heat accounted for the second term of equation (6) and third term of equation (7), respectively. Species production/depletion rate appearing in both balance equations is given by expression (8) which already includes the importance of internal diffusive limitations along the washcoat layer.

$$\dot{\omega}_{k,w} = \sum_{R=1}^{N_R}\nu_{k,R}.q_R.\eta_R.\rho_{cat.} \quad (8)$$

3.2. *Chemical kinetics*

The adopted surface chemistry scheme for catalytic partial oxidation of methane and propane fuels follows the indirect kinetic mechanism of syngas production [8,31]. Table 4 presents the kinetic model [14,19] which is composed by total oxidation (R1 and R7) and steam reforming (R2 and R8) reactions of methane and propane respectively, direct water-gas shift (R3), its reverse (R4) and consecutive H_2 and CO total oxidation reactions (R5 and R6). Reactions R7 and R8 are only considered for fuel mixtures containing propane (G21 fuel). Rate expressions for each reaction follow the Langmuir–Hinshelwood type (Table 5). The σ_k term (expression (9)) is included in each rate expression to account for the depletion of the co-reactant species in each reaction.

$$\sigma_k = \frac{P_k}{P_k + 10^{-6}} \quad (9)$$

Kinetic parameters for Arrhenius and Van't Hoff expressions are listed in Tables 6 and 7, respectively.

Surface chemistry was evaluated with surface temperature (T_s) and mixture composition at the external interface between the washcoat and the bulk gas flow ($[Y_{k,w}]$).

Table 5 – Rate expressions for each reaction.

Rate equation	Reaction
$q_{C_xH_y,tot.ox.} = \frac{k_{C_xH_y,tot.ox.}P_{C_xH_y}}{1 + k_{ads,H_2O}P_{H_2O}}\sigma_{O_2}$	R1 and R7
$q_{C_xH_y,steamref.} = \frac{k_{C_xH_y,streamref.}P_{C_xH_y}(1-\eta_{C_xH_y,streamref.})}{1 + k_{ads,CO}P_{CO} + k_{ads,O_2}P_{O_2}}\sigma_{H_2O}$	R2 and R8
$q_{DWGS} = \frac{k_{DWGS}P_{H_2O}(1-\eta_{DWGS})}{(1 + k_{ads,H_2O}P_{H_2O})^2}\sigma_{CO}$	R3
$q_{RWGS} = k_{RWGS}P_{CO_2}(1-\eta_{RWGS})\sigma_{H_2}$	R4
$q_{H_2(CO)tot.ox.} = k_{H_2(CO)tot.ox.}P_{H_2(CO)}\sigma_{O_2}$	R5 and R6

Table 6 – Kinetic parameters applied on Arrhenius expressions for each rate equation.

Reaction	A_{Ri} [mol $g_{cat.}^{-1}$ s^{-1} atm^{-1}]	$E_{act,\,Ri}$ [kJ mol^{-1}]
R1	3.2889×10^4	92
R2	3.2794×10^4	92
R3	1.9536×10^0	25
R4	6.5345×10^1	62
R5	1.3509×10^7	62
R6	6.8284×10^5	76
R7	1.5283×10^4	80
R8	3.0263×10^4	85

3.3. Transport phenomena

Heat and mass external transport coefficients (h and $K_{mat,k}$) appearing in balance equations are evaluated through Nusselt and Sherwood correlations, respectively. Since the honeycomb monolith has square shaped channels, Nusselt correlation given by expression (10) has been widely applied in literature [48]. In this correlation X^* denotes a dimensionless distance evaluated through expression (11).

$$Nu = 2.977 + \left[8.827(1000X^*)^{-0.545}\right]Exp(-48.2X^*) \tag{10}$$

$$X^* = \frac{x - x_{in}}{d_h Pe} \tag{11}$$

Sherwood number is simply given by applying the Chilton-Colburn analogy to the Nusselt correlation.

Diffusional limitations along the porous washcoat layer were considered through isothermal generalized effectiveness factors (expression (12)) computed with the generalized Thiele moduli given by expression (13), where the limiting species is denoted by k.

$$\eta_R = \frac{\tanh(\varphi_{k,R})}{\varphi_{k,R}} \tag{12}$$

$$\varphi_{k,R} = \frac{\delta_{cat.} q_R(C_k^S)\rho_{cat.}}{\sqrt{2\int_{C_k^{eq}}^{C_k^S} D_{ef,k} q_R(C_k)\rho_{cat.} dC}} \tag{13}$$

Random pore model [49] was employed to evaluate effective diffusivities considering a typical bimodal pore structure [14] with both molecular and Knudsen diffusion contributions through the Bosanquet formula. Molecular diffusion coefficients, for each diffusive limiting species, were evaluated using the Fuller-Schettler-Giddings correlation [50].

Radiative heat transfer in solid phase (fifth term of equation (7)), which also accounts for radiative heat losses near the boundaries of the catalytic monolith, was modeled through the Zone method [41] considering the gaseous mixture radiatively non-participating due to the weak radiative contribution of combustion gases [42].

In the present study, the radiative enclosure is approximated by a cylindrical channel and then surface zones are treated either as disk or ring shaped surfaces characterized by the channel hydraulic diameter. Expressions to compute shape factors between all types of surfaces were derived based on the analytical solution of two parallel and coaxial disks [51]. The inlet and outlet disk shaped surfaces represent both inlet and outlet manifolds and once the available space upstream and downstream the monolith section is relatively small a behavior different than black body is preferable for these surfaces [52,53]. Moreover, the exchange temperatures for inlet and outlet disks were kept equal to the inlet feed mixture temperature and outlet gas temperature, respectively.

After computing the direct exchange areas ($\overline{S_i S_j}$) between all pairs of surface zones (using shape factor expressions) a simple matrix manipulation [54] was then applied to obtain the total exchange areas ($\overline{S_i S_j}$) which, in a non-participating media, account for both direct radiation between surfaces as well as multiple reflections on surface zones. Finally, having already computed total exchange areas, the net radiative heat flux for each surface zone, which appears in the energy balance of solid phase, is given by expression (14).

$$q''_{s_i} = \varepsilon_i \sigma T_{s_i}^4 - \frac{1}{A_{s_i}} \sigma \sum_{j=1}^{N_s} \overline{S_j S_i} T_{s_j}^4 \tag{14}$$

Table 2 hits the emissivity values applied on the Zone method of radiative analysis.

Table 7 – Kinetic parameters applied on Van't Hoff expressions for each inhibiting species.

Species k	$A_{ads,k}$ [atm^{-1}]	$\Delta H_{ads,k}$ [kJ mol^{-1}]
O_2	2.3431×10^{-4}	−73
H_2O	4.3045×10^1	−16
CO	1.2926×10^0	−37

3.4. Geometry and boundary conditions

Two computational domains are considered since the honeycomb monolith reactor can be taken as adiabatic or non-adiabatic in the axial direction. Fig. 2a and b show the computational domains regarded. For the adiabatic reactor configuration a perfect continuity between the uncoated and catalytic monoliths is considered as well as a stepwise appearance of the washcoat layer at x = 0.0 cm.

Danckwerts type of boundary conditions applied at the inlet section for gas phase equations (expressions (15) and (16)) should be always preferable, instead of the Dirichelt boundary conditions, in all kinds of situations (with or without a front heat shield) regarding the adopted dispersion mathematical model [55]. For the energy balance of solid phase a radiative boundary condition is always considered (expression (17)).

At the catalyst exit section zero-Neumann type of boundary conditions (expressions (18), (19) and (20)) are applied to all steady-state differential equations since all gradients become insignificant.

Inlet section

$$u(Y_{k,g} - Y_{k,in}) - D_{k,g}\frac{\partial Y_{k,g}}{\partial x} = 0 \tag{15}$$

$$\rho_g C_{p,g} u(T_g - T_{g,in}) - k_g \frac{\partial T_g}{\partial x} = 0 \tag{16}$$

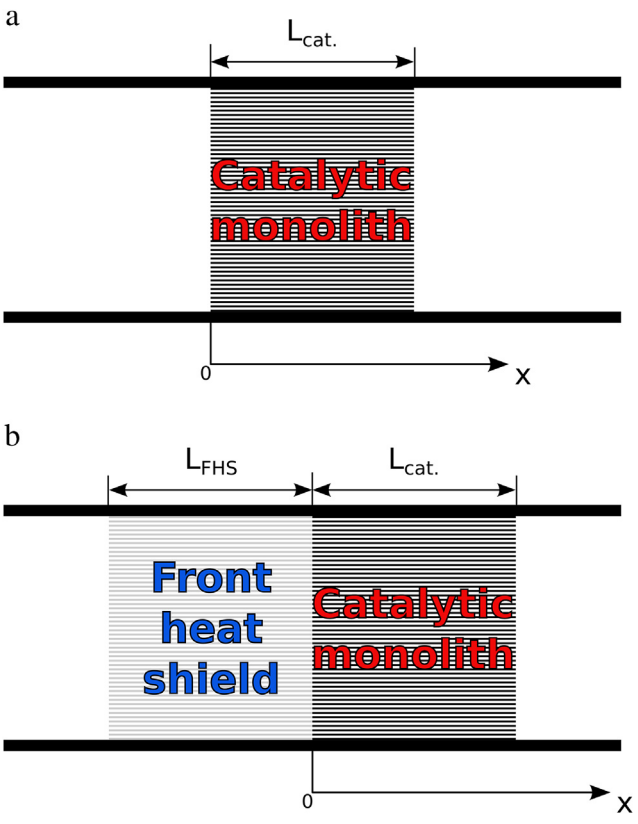

Fig. 2 – Schematic representation of the computational domains: a) non-adiabatic monolith reactor configuration; b) adiabatic monolith reactor configuration. $L_{FHS} = L_{cat.} = 2.0$ cm

$$k_s \frac{\partial T_s}{\partial x} - \sigma \varepsilon_s \left(T_s^4 - T_{g,in}^4 \right) = 0 \quad (17)$$

Outlet section

$$\frac{\partial Y_{k,g}}{\partial x} = 0 \quad (18)$$

$$\frac{\partial T_g}{\partial x} = 0 \quad (19)$$

$$\frac{\partial T_s}{\partial x} = 0 \quad (20)$$

3.5. *Numerical model*

The present mathematical model was implemented in an in-house version of PREMIX code [56] from CHEMKIN family combustion codes. To reduce the boundary value problem to a system of non-linear algebraic equations finite difference approximations are employed. Then on a uniform coarse initial mesh the program attempts to solve the problem through a damped Newton's method. An adaptive mesh procedure based on gradient and curvature resolutions between gridpoints is always applied to reach finner meshes after a converged solution on a previous mesh is attained. If the solution lies out of the steady-state domain of convergence a time-stepping procedure is also applied to bring the solution into steady-state domain of convergence of Newton's method.

All thermodynamic and transport data were evaluated using CHEMKIN correlations [45,57] with thermodynamic and transport coefficients given by GRI-Mech 3.0 database [58].

4. Results

4.1. *Model validation*

The catalytic reactor was investigated experimentally at atmospheric pressure and steady-state conditions for pure methane (G20) and two different fuel mixtures: 85% CH_4 + 15% N_2 (G231) and 87% CH_4 + 13% C_3H_8 (G21). The experimental species concentration and temperature data for each specific operating condition is hereafter employed to validate model predictions.

4.1.1. *G20: pure methane*

Four different volumetric fuel flow rates (2, 4, 6 and 8 NL/min) were experimentally investigated with a constant air to fuel equivalence ratio ($\lambda = 0.31$) and for two inlet reformer temperatures (350 °C and 300 °C), being the lowest temperature applied to the two higher values of fuel flow rate (6 and 8 NL/min) to shift the thermal behavior of the reactor away from the thermal deactivation regime.

Fig. 3a and b show the comparison between numerical and experimental thermal profiles along the catalyst bed for inlet temperatures of 350 °C and 300 °C, respectively. A good matching between experimental and numerical results is well visible.

The solid and gas temperatures increase with the fuel flow rate, almost uniformly along the catalyst axial length, due to an increase in the chemical net heat release. Furthermore, both temperatures increase with fuel flow rate particularly for lower ranges of fuel rates (Fig. 3a) because the relative heat losses (by radiation) are higher for low fuel flow rates than for high fuel flow rates. An increase in the fuel flow rate also promotes a decoupling between both thermal profiles at the inlet region of the catalyst bed, which in turn influences the axial location where the maximum gas temperature is registered and the length required to attain thermal equilibrium between phases. However, since the washcoat layer was assumed to start at the reactor inlet ($x = 0.0$ cm), the maximum catalyst surface temperature is always located very near this section.

The integral product distribution is listed in Table 8 denoting a good agreement between all the measured and predicted species for all the fuel flow rates investigated.

4.1.2. *G231: 85% methane + 15% nitrogen*

The measured and predicted solid and gas temperatures along the monolith are compared in Fig. 4a and b. Fig. 4a shows that the gas and solid temperatures increase with the air to fuel equivalence ratio. Moreover the mixture composition, calculated and measured, at the exit section (Table 9) denotes a decreasing trend toward synthesis gas selectivity whereas higher values of fuel conversion are noticed when

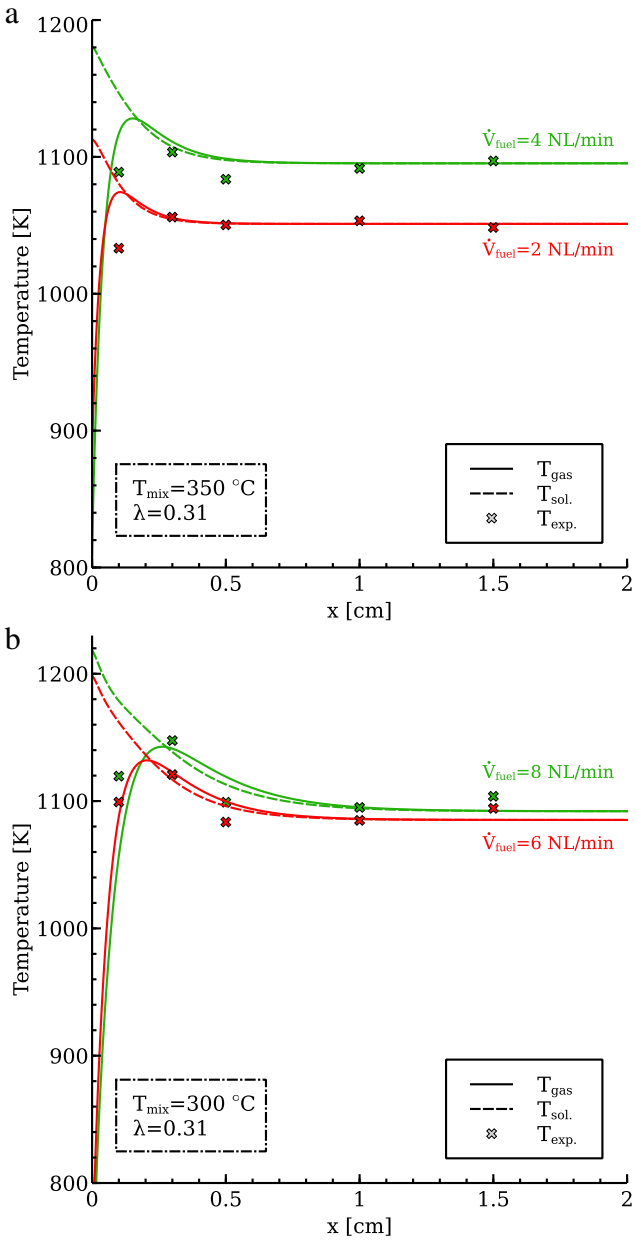

Fig. 3 – Numerical and experimental temperature profiles for different fuel flow rates considering an air to fuel equivalence ratio of 0.31 and two inlet reformer temperatures: a) T_{mix} = 350 °C; b) T_{mix} = 300 °C.

increasing the air to fuel equivalence ratio. These trends are justified with an increasing shift on the global reaction stoichiometry from partial to total oxidation when the air to fuel equivalence ratio is increased [8]. In addition, the thermal equilibrium length increases with a decrease on air to fuel equivalence ratio. Regarding fuel flow rate influence on reactor behavior, Fig. 4b depicts similar conclusions of the previous G20 fuel, namely the increase of temperature with fuel rate and the axial location of the thermal equilibrium regime between phases which occurs further downstream the reactor.

Table 8 – Numerical and experimental integral species molar fractions (on a dry basis) for all operating conditions assessed with G20 fuel.

T_{mix} [°C]	$\dot{V}_{fuel}$ [NL/min]	λ [–]		X [%]				
				H_2	CO	CO_2	CH_4	N_2
350	2	0.31	Num.	35.4	17.3	1.8	0.2	45.3
			Exp.	33.2	15.6	3.3	0.7	47.2
	4	0.31	Num.	35.5	17.8	1.6	0.1	45.0
			Exp.	35.1	17.1	2.4	0.2	45.2
300	6	0.31	Num.	35.5	17.6	1.7	0.1	45.2
			Exp.	35.7	17.4	2.1	0.2	44.6
	8	0.31	Num.	35.5	17.8	1.6	0.1	45.1
			Exp.	35.9	17.5	2.0	0.1	44.5

4.1.3. *G21: 87% methane + 13% propane*

Fig. 5a and b compare the measured and predicted solid temperatures for inlet gas temperatures of 300 °C and 350 °C, respectively, but only the temperature measured by the thermocouple placed at x = 1.5 cm is available for validation purposes. An increase on air to fuel equivalence ratio increases the temperature at x = 1.5 cm as well as the methane conversion at the catalyst exit section (Table 10) while the molar fraction of partial oxidation species has a decreasing trend. No traces of propane were found at the outlet section. The trends on temperature and integral product distribution herein observed with an air to fuel equivalence ratio variation are in agreement with the previous findings for G231 fuel.

From the comparison between numerical and experimental data for the three fuel mixtures shown above, one can conclude that the present model is able to predict the main features of methane and propane CPOx to investigate non-adiabatic honeycomb monolith configurations.

4.2. *Radiative heat losses*

The influence of fuel flow rate and air to fuel equivalence ratio on the role of radiative heat transfer in the non-adiabatic reactor performance is investigated with G20 as the reference fuel.

4.2.1. *Effect of fuel flow rate*

The influence of the fuel flow rate on radiative heat losses was investigated in the range of 2–6 NL/min for an air to fuel equivalence ratio of 0.31 and for an inlet gas temperature of 300 °C.

Fig. 6a shows that under adiabatic conditions an increase in fuel flow rate decreases the importance of solid conduction along the front heat shield due to an enhancement of convective heat transfer [31]. Moreover, when increasing the fuel flow rate the maximum surface and gas temperatures, which are achieved near the inlet section of the catalytic region, increase and move downwards (specially remarkable for the gas temperature profile).

Even being denoted as the "adiabatic reactor configuration", the adiabaticity of this reactor arrangement also presents a slight dependence on the fuel flow rate, specially for the lowest fuel flow rate considered (2 NL/min). Under these

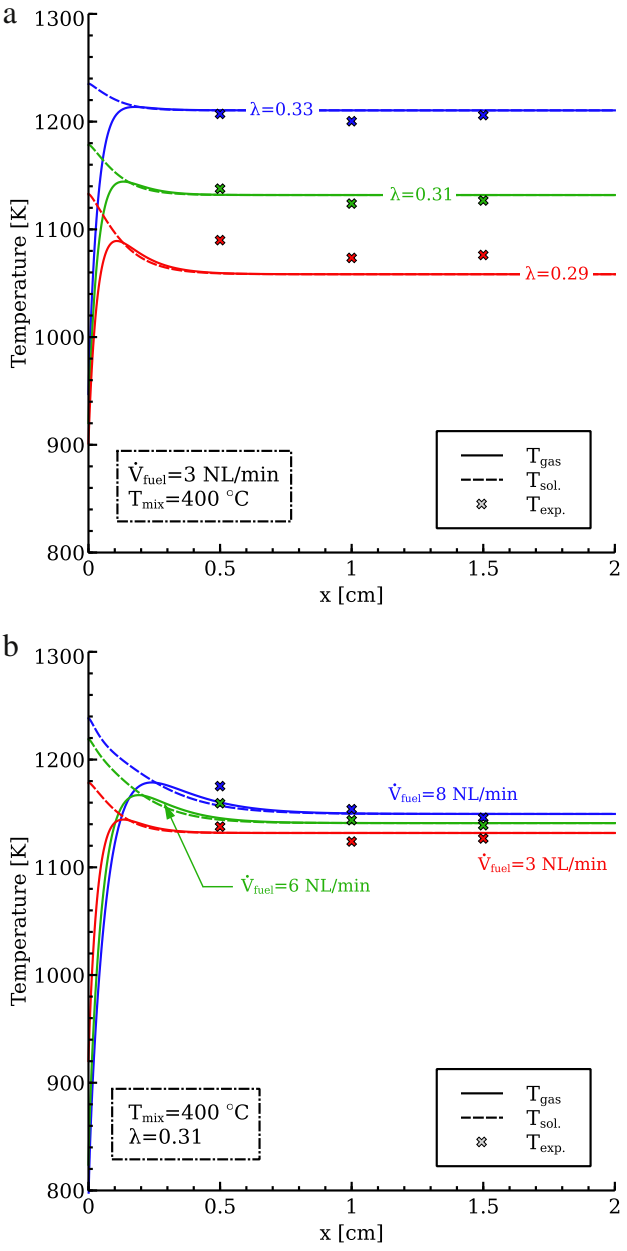

Fig. 4 – Numerical and experimental temperature profiles: a) for different air to fuel equivalence ratio values with T_{mix}=400 °C and $\dot{V}_{fuel}$=3 NL/min; b) for different fuel flow rate values with T_{mix}=400 °C and λ=0.31.

circumstances, the solid conduction along the front heat shield is responsible for a small radiative heat loss from the inlet section of the monolith reactor (Fig. 6a). Ultimately, this non-perfect adiabatic behavior will lead to a slightly lower outlet gas temperature comparing to the adiabatic temperature rise attained for higher fuel flow rates. For low fuel flow rates an improvement of the reactor adiabaticity can be somewhat achieved increasing the heat shield length or decreasing its thermal conductivity. However a decrease in the thermal conductivity of the front heat shield expectably increases the maximum solid temperature (see [30]).

Table 9 – Numerical and experimental integral species molar fractions (on a dry basis) for all operating conditions assessed with G231 fuel.

$\dot{V}_{fuel}$ [NL/min]	T_{mix} [°C]	λ [–]		X [%]				
				H_2	CO	CO_2	CH_4	N_2
3	400	0.29	Num.	35.3	17.4	1.3	0.3	45.7
			Exp.	34.9	16.9	2.4	0.3	45.5
		0.31	Num.	33.9	17.1	1.6	0.0	47.4
			Exp.	33.9	16.7	2.6	0.1	46.7
		0.33	Num.	32.1	16.5	1.7	0.0	49.7
			Exp.	32.0	16.0	3.0	0.0	49.0
6	400	0.31	Num.	34.4	17.3	1.3	0.0	47.0
			Exp.	34.6	17.3	2.1	0.1	45.9
8	400	0.31	Num.	34.3	17.3	1.3	0.0	47.1
			Exp.	34.8	17.4	1.9	0.1	45.8

The thermal profiles for the non-adiabatic monolith reactor, presented in Fig. 6b, show that an increase in fuel flow rate results in higher temperatures, not only in the beginning of the catalyst bed but also along the whole catalyst length. Therefore, the outlet gas temperatures achieved at non-adiabatic conditions are highly dependent on the applied fuel rate and they tend to approach the adiabatic temperature for high fuel flow rates.

For both adiabatic and non-adiabatic cases the maximum values of surface temperature increase with fuel flow rate. However, this increase is not linear because the heat release from surface reactions also increases but the heat conduction, convection and radiation are no longer able to remove efficiently the heat generated. Moreover, the approach to the thermodynamic equilibrium, which was verified for all fuel rates in Fig. 6a and b, is favored by low fuel flow rates, since increasing the fuel flow rate a longer catalyst is required to achieve thermodynamic equilibrium conditions.

For direct comparison between maximum surfaces temperatures, achieved under adiabatic and non-adiabatic operation, the maximum surface temperatures of the adiabatic case are also presented in Fig. 6b. The non-adiabatic reactor configuration has the potential to decrease maximum surface temperatures for low fuel flow rates in relation to the adiabatic operation, as recently corroborated by experimental findings [44]. For higher fuel flow rates the maximum surface temperature differences decrease and in particular for 6 NL/min the maximum surface temperature observed for the non-adiabatic case is even higher than the respective adiabatic value. This is largely due to the fact that increasing the input power the heat transfer mechanisms available to scatter the heat release are less efficient in the non-adiabatic case than in the adiabatic reactor configuration. However, it is worth noting that a better non-adiabatic thermal performance can be accomplished by proper choosing several geometrical properties (hydraulic diameter and cell density) and thermophysical properties (solid conductivity and surface emissivities).

Fig. 7a and b show the net radiative heat fluxes along the channel for the adiabatic and non-adiabatic reactors. Due to the high surface temperature and thermal gradients established in the first few millimeters of the catalyst region (Fig. 6), the radiant heat exchange becomes extremely important in

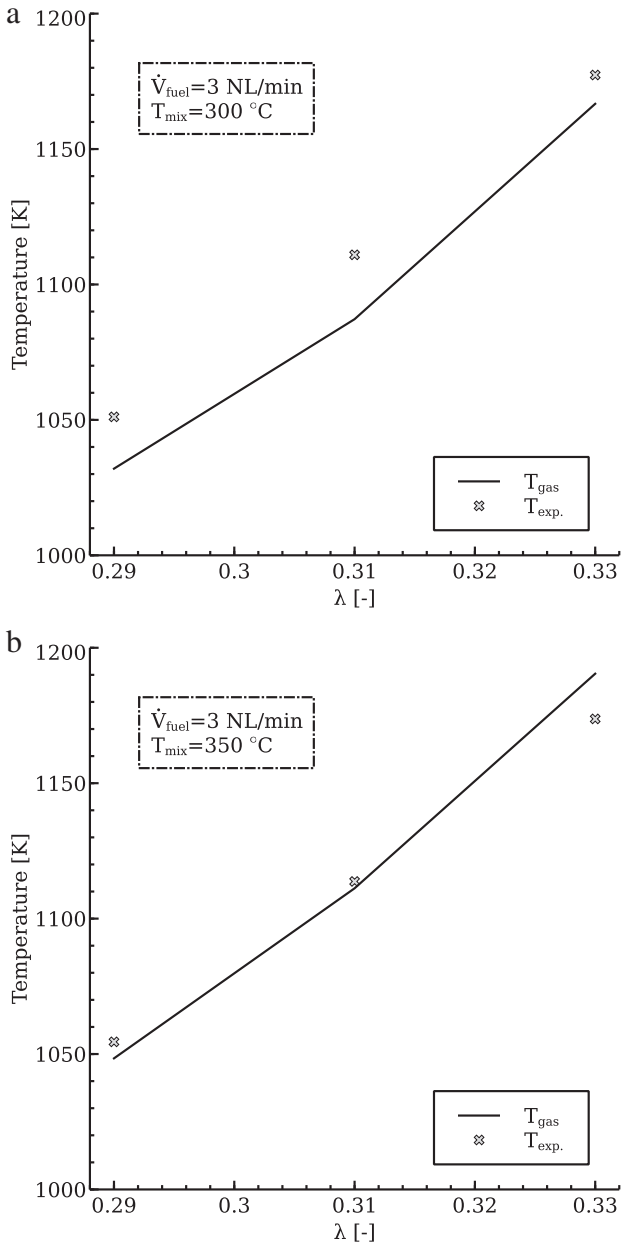

Fig. 5 – Numerical and experimental temperatures at x=1.5 cm for different air to fuel equivalence ratio values considering a fuel flow rate of 3 NL/min and two inlet reformer temperatures: a) T_{mix}=300 °C; b) T_{mix}=350 °C.

this region. Furthermore, as the fuel flow rate increases also the importance of radiative heat transport increases which means that for the non-adiabatic case (Fig. 7b) higher heat fluxes are lost from the inner channel walls to the inlet surroundings. However, for the adiabatic configuration near the inlet section of the front heat shield (x = −2.0 cm) the radiative heat transport becomes negligible and then the heat losses from the channel walls are not important (Fig. 7a).

We define a parameter Ω, see expression (21), as the ratio between the overall radiative heat losses from the reactor and the chemical heat release and we call it relative radiative heat losses.

Table 10 – Numerical and experimental integral species molar fractions (on a dry basis) for all operating conditions assessed with G21 fuel.

$\dot{V}_{fuel}$ [NL/min]	T_{mix} [°C]	λ [–]		X [%]				
				H_2	CO	CO_2	CH_4	N_2
3		0.29	Num.	34.9	19.2	1.2	0.8	43.9
			Exp.	34.4	19.0	2.0	0.7	43.9
	300	0.31	Num.	34.2	19.0	1.3	0.1	45.4
			Exp.	33.7	18.8	2.3	0.2	45.0
		0.33	Num.	32.6	18.5	1.6	0.0	47.3
			Exp.	32.3	18.1	2.7	0.0	46.9
		0.29	Num.	35.3	19.5	1.0	0.5	43.7
			Exp.	34.4	18.8	2.0	0.7	44.1
	350	0.31	Num.	34.3	19.2	1.3	0.1	45.1
			Exp.	33.6	18.4	2.3	0.2	45.5
		0.33	Num.	32.6	18.5	1.6	0.0	47.3
			Exp.	32.1	17.9	2.8	0.0	47.2

$$\Omega = \frac{A\dot{q}_{rad_{loss}}}{A\int_{L_{cat.}} \xi \sum_{k=1}^{KK_w} \dot{\omega}_{k,w} H_k(x)\mathrm{d}x} \tag{21}$$

Fig. 8 shows that the relative radiative heat losses from the non-adiabatic monolith decrease with increasing values of fuel flow rate because the chemical heat release dominates over radiative energy losses.

The chemical heat release ($\dot{q}_{chem.}$) evaluated with the denominator of expression (21) is also plotted in Fig. 8 as a function of the fuel flow rate. A higher chemical heat release presented for the non-adiabatic configuration suggests that the global reaction pathway for the non-adiabatic cases proceeds preferentially through exothermic reactions. However, the net heat release ($\dot{q}_{net} = \dot{q}_{chem.} - \dot{q}_{rad_{loss}}$) noticed for the non-adiabatic case is always lower than the adiabatic net heat release ($\dot{q}_{net} = \dot{q}_{chem.}$) which justifies the general lower temperatures observed at non-adiabatic conditions (Fig. 6). Furthermore, the net heat release of the non-adiabatic monolith increases with fuel flow rate and tends to approach the adiabatic chemical heat release for the same values of fuel rate that assure a non-adiabatic outlet temperature closer to the adiabatic temperature (see Fig. 6b).

Besides the thermal evolution along the reactor, the reforming performance is commonly assessed through several key parameters such as fuel conversion (X_{CH_4}), syngas selectivities (S_{H_2} and S_{CO}) and total reforming efficiency ($\eta_{ref.}$). These parameters are evaluated through the following expressions at the outlet catalyst section:

$$X_{CH_4} = \frac{(\dot{n}_{CH_4})_{in} - (\dot{n}_{CH_4})_{out}}{(\dot{n}_{CH_4})_{in}} \times 100\% \tag{22}$$

$$S_{CO} = \frac{\dot{n}_{CO}}{\dot{n}_{CO} + \dot{n}_{CO_2}} \times 100\% \tag{23}$$

$$S_{H_2} = \frac{\dot{n}_{H_2}}{\dot{n}_{H_2} + \dot{n}_{H_2O}} \times 100\% \tag{24}$$

$$\eta_{ref.} = \frac{\dot{n}_{H_2} LHV_{H_2} + \dot{n}_{CO} LHV_{CO}}{\dot{n}_{fuel} LHV_{fuel}} \times 100\% \tag{25}$$

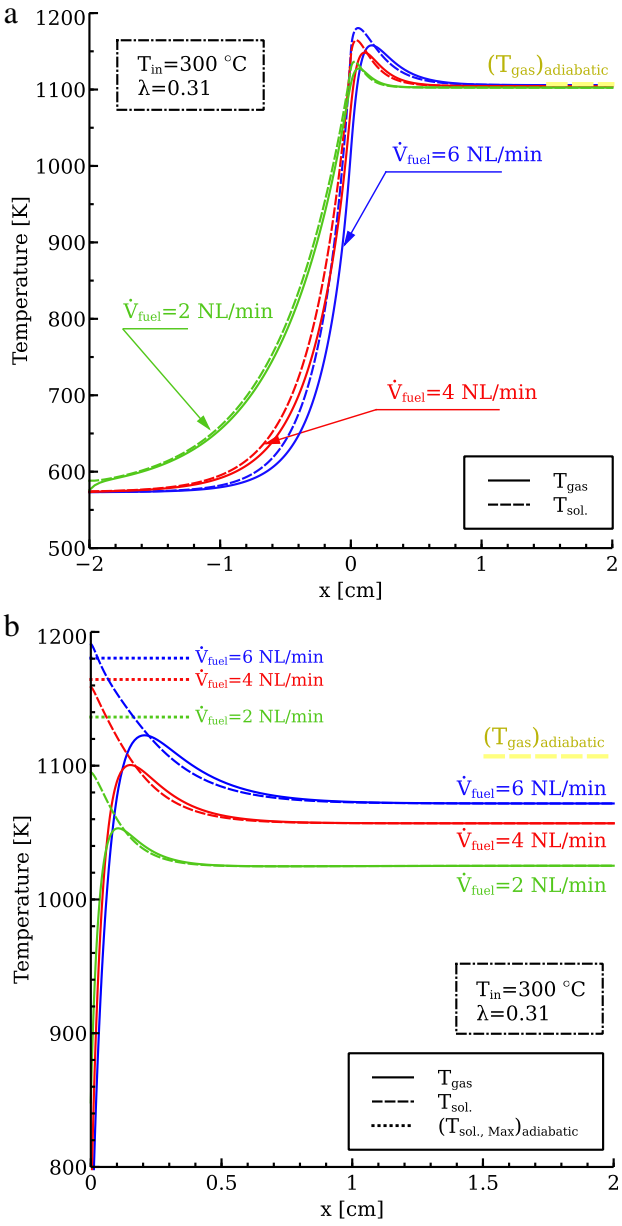

Fig. 6 – Thermal profiles of adiabatic (a) and non-adiabatic (b) reactor configurations for different fuel flow rates.

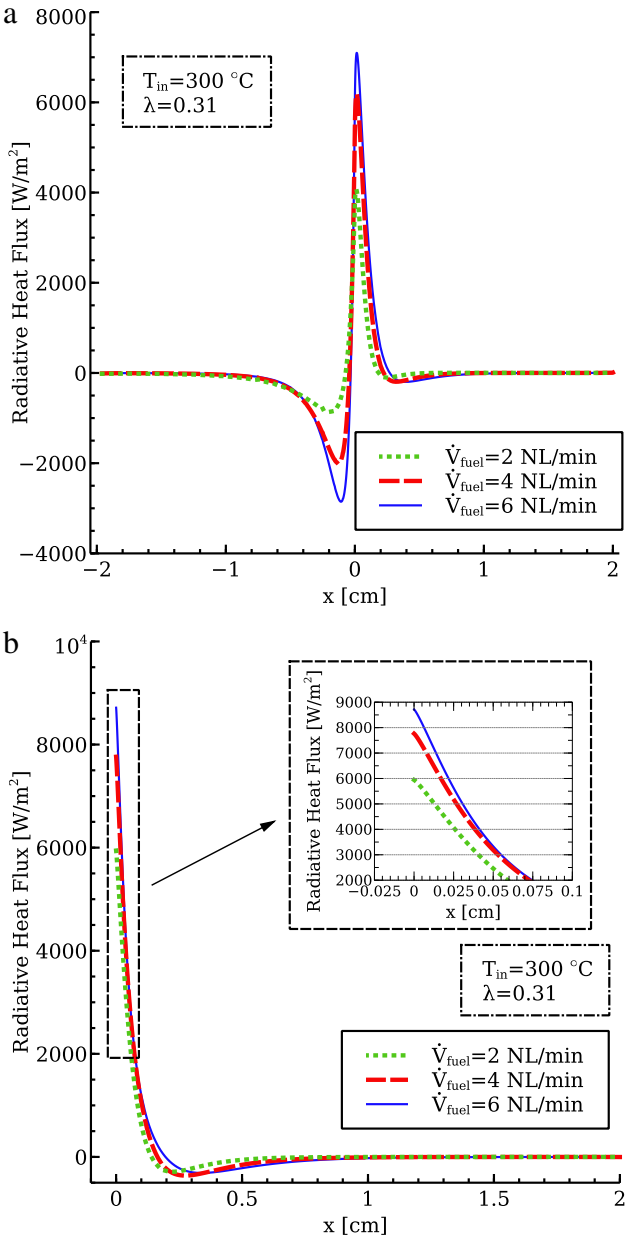

Fig. 7 – Net radiative heat fluxes along channel walls for different fuel flow rates: a) adiabatic monolith; b) non-adiabatic monolith.

Fig. 9a shows that for the adiabatic reactor configuration the performance parameters are nearly independent of the fuel flow rate, since the heat losses are not meaningful and thermodynamic equilibrium is reached before the outlet section. Regarding the non-adiabatic cases, the parameters increase with fuel flow rate, except the hydrogen selectivity which presents a nearly constant value for the fuel flow rates considered. The H_2/CO molar ratio is also plotted in Fig. 9a showing, for the non-adiabatic case, a decreasing tendency with fuel flow rate. The adiabatic values of fuel conversion, reforming efficiency and CO selectivity are higher than those achieved through non-adiabatic reactor operation but the H_2/CO ratio obtained in non-adiabatic operation is slightly higher than that accomplished by an adiabatic operation.

The non-adiabatic H_2 selectivity trend observed in Fig. 9a requires an inspection for other air to fuel equivalence ratio values. Fig. 9b presents the evolution of S_{H_2} for three different air to fuel equivalence ratio values. The non-adiabatic H_2 selectivity increases for low air to fuel equivalence ratios ($\lambda = 0.29$) with fuel flow rate but never exceeds the values achieved for the adiabatic cases. However, a completely different trend is visible for higher air to fuel equivalence ratios ($\lambda = 0.33$) since the S_{H_2} decreases with fuel flow rate but with higher values than the adiabatic cases. Thus, regarding hydrogen selectivity as the fuel flow rate increases the non-adiabatic reactor performance approaches the adiabatic from lower values of S_{H_2} for low air to

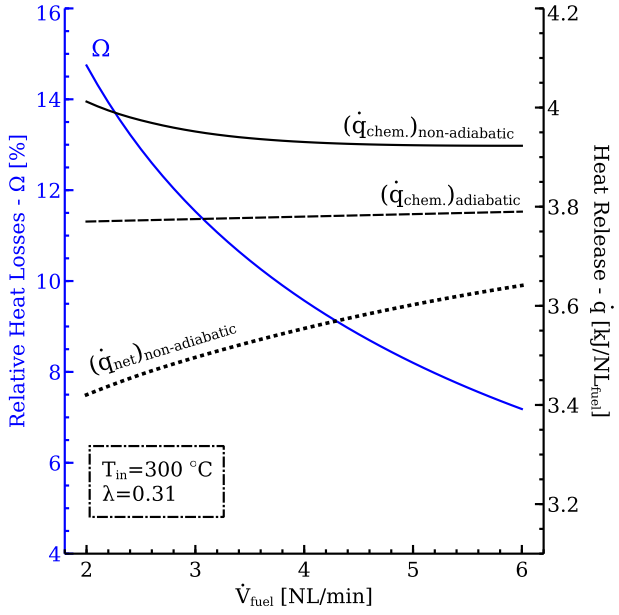

Fig. 8 – Importance of overall radiative heat losses for different fuel flow rates.

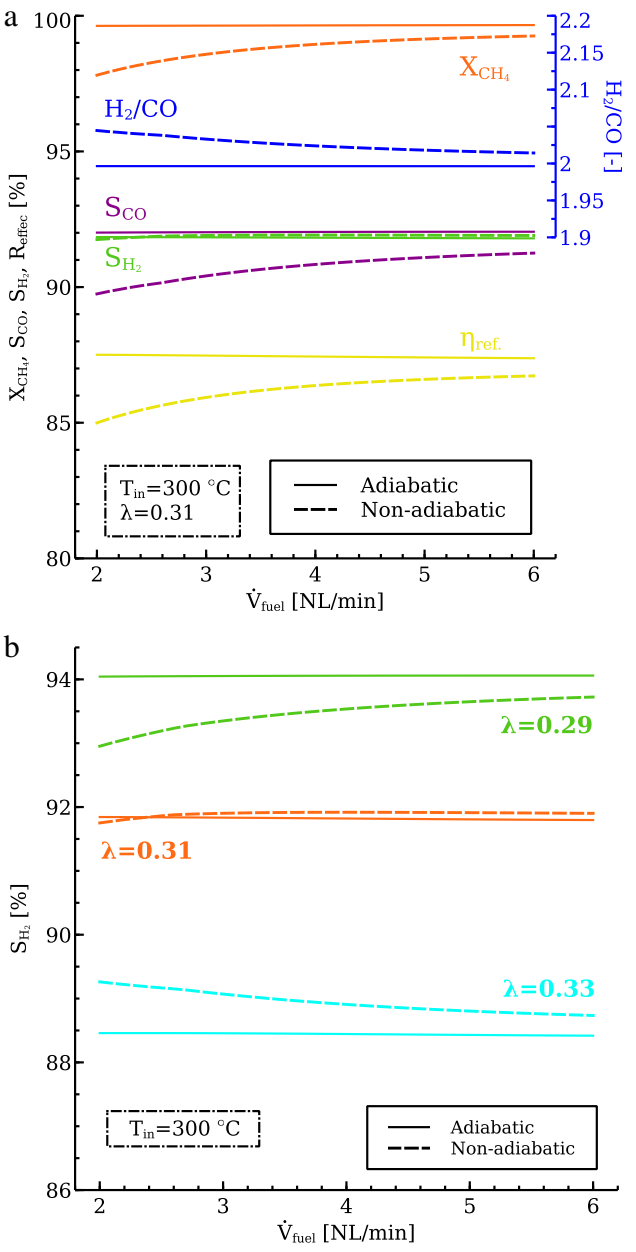

Fig. 9 – Performance parameters achieved for both reactor operation modes with fuel flow rate: a) fuel conversion, CO and H_2 selectivities, reformer total efficiency and H_2/CO molar ratio; b) H_2 selectivities for three different air to fuel equivalence ratios.

fuel equivalence ratios and from higher values for high air to fuel equivalence ratios.

For an air to fuel equivalence ratio of 0.33 the higher H_2 selectivity observed at non-adiabatic conditions is mainly motivated by a different overall behavior of the water-gas shift (WGS) reaction. Under non-adiabatic conditions the equilibrium of the WGS reaction is shifted toward the production of H_2 which simultaneously contributes to lower the H_2O integral production in such a way that the H_2 selectivity is increased.

4.2.2. *Effect of air to fuel equivalence ratio*

To further analyze the role of radiative heat losses in the non-adiabatic reactor behavior an air to fuel equivalence ratio ranging from 0.29 to 0.33 was herein employed together with a constant fuel flow rate (4 NL/min) and inlet gas temperature (300 °C).

Fig. 10a and b show that increasing the air to fuel equivalence ratio the temperature along the catalyst increases, mainly due to a progressive shift from partial (slightly exothermic) to total oxidation (strongly exothermic reaction) [8]. The thermodynamic equilibrium, as the air to fuel equivalence ratio increases, is reached earlier for both reactor configurations. The differences in the outlet temperatures observed for the adiabatic monolith (Fig. 10a) are due to the mixture composition that varies with the air to fuel equivalence ratio. The temperature at the exit section achieved in the adiabatic configuration approaches the adiabatic value for each air to fuel equivalence ratio considered which points out negligible heat losses. For the non-adiabatic reactor configuration as the air to fuel equivalence ratio increases the outlet temperature deviates from the adiabatic value. Fig. 10b also shows, in the air to fuel equivalence ratio range considered, that the maximum surface temperatures achieved in the non-adiabatic reactor configuration are in general lower than those observed in the adiabatic cases. Moreover as the air to fuel equivalence ratio increases the non-adiabatic operation becomes more profitable to reduce hot spot formation.

At the catalytic inlet section of both reactor configurations the solid temperatures increase with air to fuel equivalence ratio leading to a higher importance of radiative heat transfer in this region which in the non-adiabatic case will be responsible for high heat fluxes lost from the reactor walls. Fig. 11 shows that upon increasing the air to fuel equivalence ratio the relative radiative heat losses (Ω) slightly decrease but the net heat release achieved during non-adiabatic operation

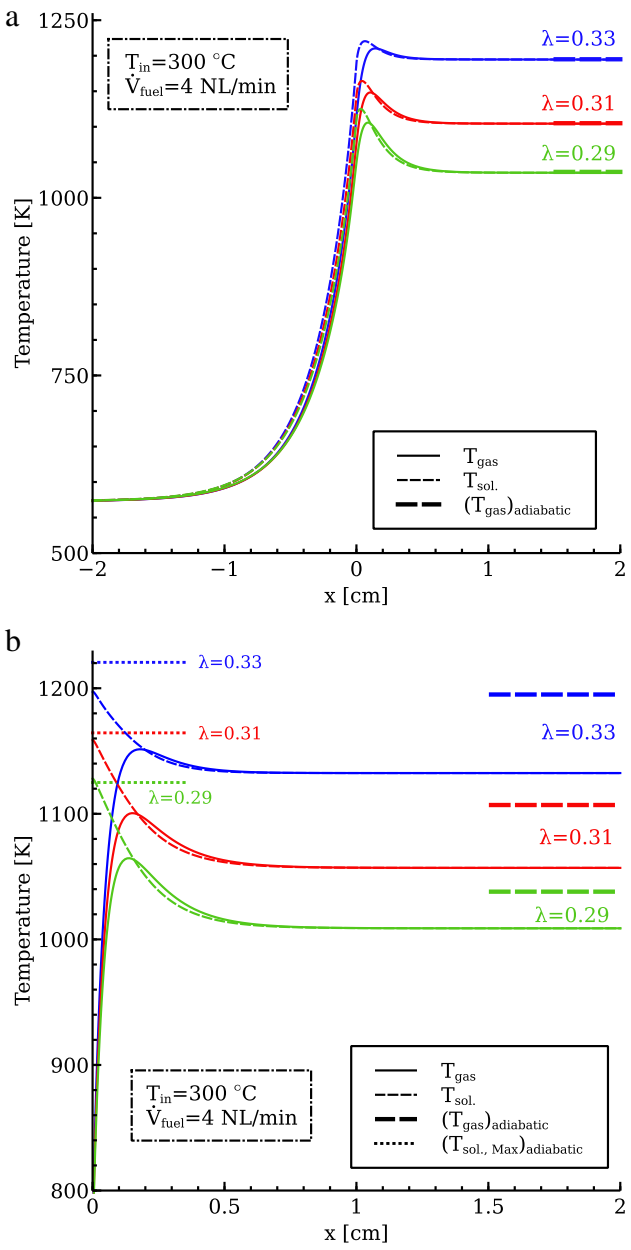

Fig. 10 – Thermal profiles of adiabatic (a) and non-adiabatic (b) reactor configurations for different air to fuel equivalence ratios.

deviates from the adiabatic chemical heat release. Therefore, as the air to fuel equivalence ratio increases the outlet gas temperature obtained at non-adiabatic conditions increasingly deviates from the adiabatic temperature rise (see Fig. 10b).

Fig. 12 shows the trends of performance parameters as a function of the air to fuel equivalence ratio for the adiabatic and non-adiabatic reactor configurations. A similar evolution with air to fuel equivalence ratio for fuel conversion, syngas selectivity and H_2/CO ratio is observed. The adiabatic case presents always more favorable values for the evaluated performance parameters with the exception for H_2/CO ratio and H_2 selectivity at higher air to fuel equivalence ratios.

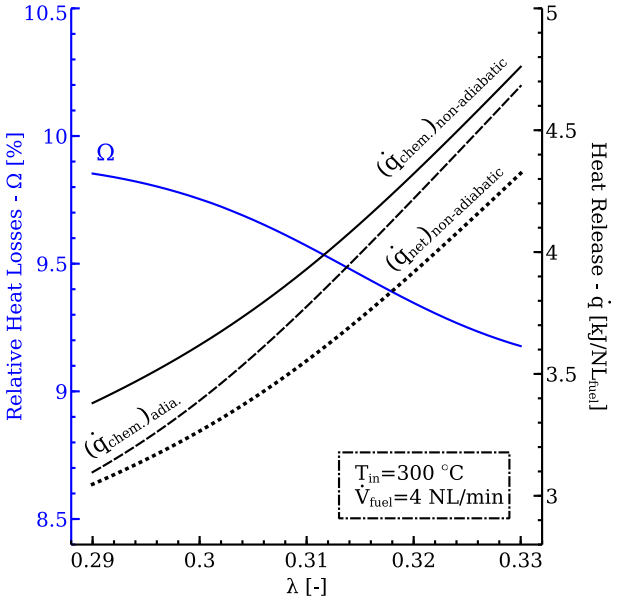

Fig. 11 – Importance of overall radiative heat losses for different air to fuel equivalence ratios.

4.2.3. *Effect of fuel composition*

A constant inlet reactor temperature of 300 °C and a C/O ratio of 0.8 were considered. The performance of the reactor fueled with G20 is taken as reference for comparison purposes.

Concerning the adiabatic case, Fig. 13a shows lower temperatures achieved with G231 fuel independently of the employed fuel rate. The addition of an inert species, such as

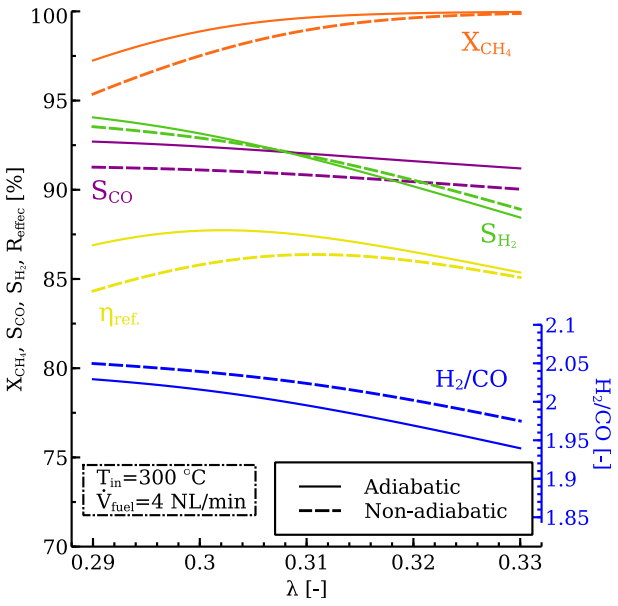

Fig. 12 – Fuel conversion, CO and H_2 selectivities, reformer total efficiency and H_2/CO molar ratio for both reactor operation modes under different air to fuel equivalence ratio values.

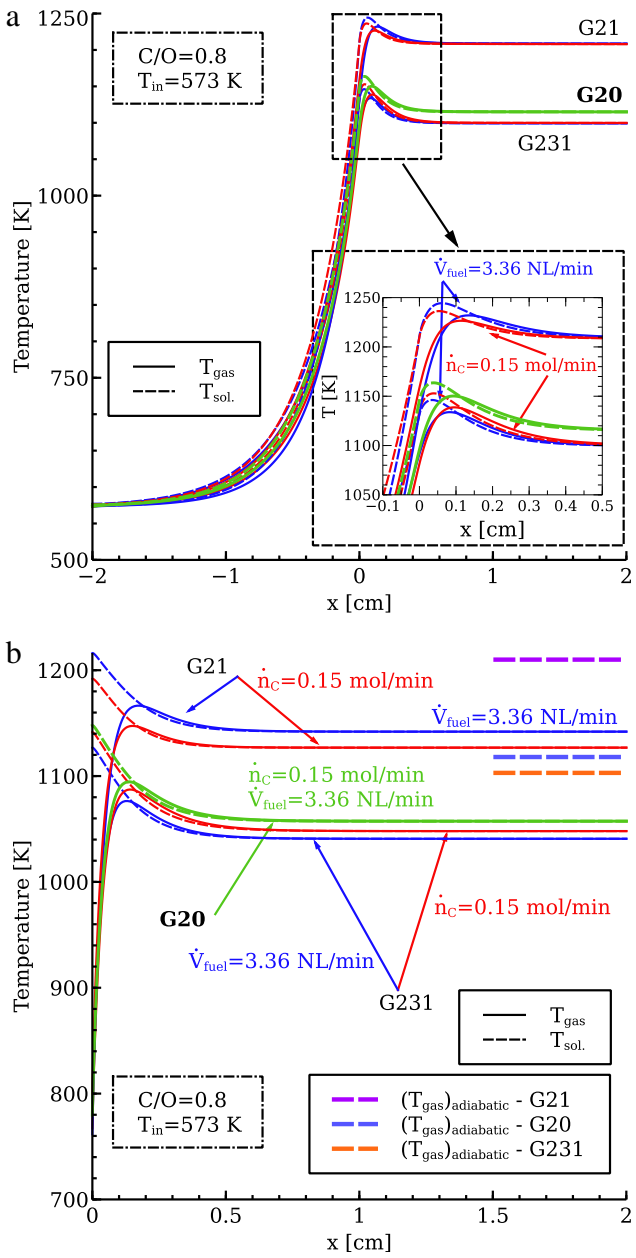

Fig. 13 – Thermal profiles of adiabatic (a) and non-adiabatic (b) reactor configurations for different fuel mixtures.

N_2 to methane, increases the specific heat of the mixture for the same amount of heat release. Donazzi et al. [34] explored the addition of N_2 on methane CPOx with a constant C/O ratio (≈0.9) and total flow rate (10 NL/min) through axial detailed measurements of gas temperature and a significant decrease of gas temperatures were evidenced by increasing methane dilution. Higher temperatures are noticed for G21 fuel due to the higher exothermicity of the global G21 CPOx reaction ($(\Delta H_R^\circ)_{G21} = -61$ kJ mol^{-1} vs. $(\Delta H_R^\circ)_{G20} = -36$ kJ mol^{-1}).

For G20 a fuel flow rate of 3.36 NL/min was chosen corresponding to a carbon molar flow rate ($\dot{n}_C$) of 0.15 mol/min and for the remaining fuels two flow rates were investigated: the achieved with the same $\dot{n}_C$ applied on G20 case (case A) and $\dot{V}_{fuel} = 3.36$ NL/min (case B). Table 11 presents the fuel flow rate values for each fuel and case study.

For the adiabatic monolith (Fig. 13a) the differences between case A and case B are mainly observable near the catalytic inlet section and along the front heat shield due to the different importance of thermal conduction as previously concluded.

For the non-adiabatic reactor with G231 fuel and regarding case A the methane molar flux that is present in the fuel feed stream is equal to the G20 case and as one can see in Fig. 13b lower temperatures for G231 with case A are highlighted. For G231 fuel with case B even lower temperatures are observed due to a decrease of the fuel flow rate which points out a higher importance of radiative heat losses in case B than case A (see Ω in Table 11). Regarding G21 fuel, higher temperatures are noticed for both cases in relation to G20 fuel. Table 11 shows for the non-adiabatic monolith, with G231 and G21 fuels, a decreasing tendency of relative radiative heat losses (Ω) with an increase on fuel flow rate. This is in full agreement with the previous section about the influence of the fuel flow rate on the adiabaticity of the reactor for G20 fuel. Therefore, as the Ω decreases the net heat release ($(\dot{q}_{net})_{non-adia.}$) increases toward the chemical heat release obtained at adiabatic conditions ($(\dot{q}_{chem.})_{adia.}$) and the non-adiabatic thermal behavior approaches that achieved at adiabatic conditions, in particular near the outlet catalyst section (see Fig. 13b). It is also observed in Table 11 that fuels with higher power density display during non-adiabatic operation a lower relative radiative heat loss for a constant fuel flow rate.

Table 11 also shows that, among the fuel samples considered, G21 fuel allows the most significant decrease in the maximum surface temperature during the non-adiabatic operation (last row of Table 11). The role of the fuel flow rate to maximize the temperature difference is similar for all fuels analyzed - as the fuel flow rate increases the non-adiabatic behavior becomes less favorable to decrease hot spot formation.

Fig. 14a presents for all the fuels under consideration a higher H_2 selectivity for the non-adiabatic reactor than for the adiabatic case (more striking for G21 fuel). An opposite trend is observed for the CO selectivity. G21 fuel shows, independently of the reactor insulation, the lowest S_{H_2} and the highest S_{CO} and consequently is the fuel with the lowest H_2/CO ratio. The H_2/CO ratio observed for G231 fuel is slightly higher than for G20 which is also in agreement with Donazzi et al. [34].

Table 11 – Importance of radiative heat losses for each fuel considering different fuel flow rates.

Fuel	G20	G231		G21	
Case study	A/B	A	B	A	B
$\dot{V}_{fuel}$ [NL/min]	3.36	3.95	3.36	2.67	3.36
$(\dot{q}_{chem.})_{adia.}$ [kJ/NL$_{fuel}$]	3.88	3.31		5.70	
$(\dot{q}_{net})_{non-adia.}$ [kJ/NL$_{fuel}$]	3.60	3.09	3.06	5.13	5.23
Ω [%]	10.68	10.37	11.51	11.13	9.60
$(T_{sol.,Max})_{adia.} - (T_{sol.,Max})_{non-adia.}$ [K]	15.87	11.48	19.34	44.41	28.13

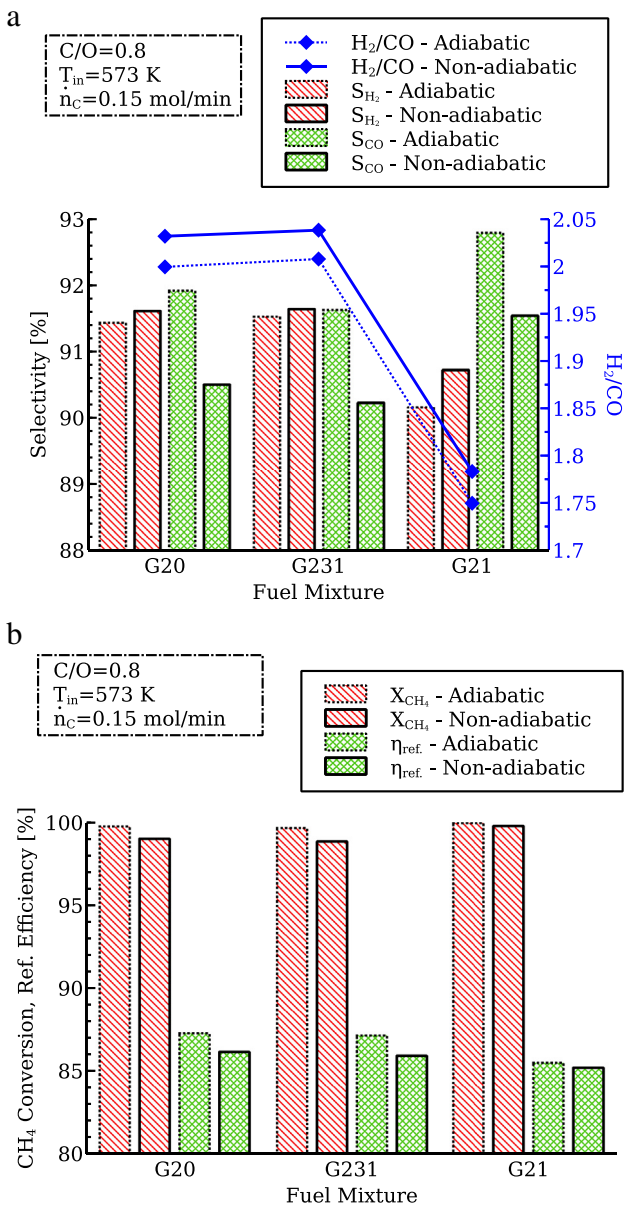

Fig. 14 – Integral adiabatic and non-adiabatic reactor performances: a) H_2 and CO selectivities and H_2/CO molar ratio; b) CH_4 conversion and total reforming efficiency.

Fig. 14b shows that for the three fuel mixtures the adiabatic monolith assures higher values of methane conversion and reforming efficiency than the non-adiabatic configuration.

5. Conclusions

An experimental and numerical investigation of catalytic partial oxidation of hydrocarbons was performed for three different fuel compositions representative of natural gas (pure methane - G20 fuel, 85% CH_4 + 15% N_2 - G231 fuel and 87% CH_4 + 13% C_3H_8 - G21 fuel) in a non-adiabatic honeycomb monolith reactor. A heterogeneous mathematical 1D model taking into account the coupling between heat and mass transport and surface chemistry was successfully validated against temperature and concentration measurements.

The model was applied to explore the effect of fuel flow rate, air to fuel equivalence ratio and fuel composition on the radiative heat losses through comparisons of the non-adiabatic and adiabatic reactor configurations. On the range of operating conditions considered, the results show that:

- radiative heat losses promoted a significant decrease of the maximum surface temperature relatively to the adiabatic case, namely for low fuel flow rates, high air to fuel equivalence ratios and for fuels with high power densities ($LHV_{G21} > LHV_{G20} > LHV_{G231}$). Opposite trends on operating conditions may lead to a higher surface maximum temperature in the non-adiabatic case compared to the adiabatic reactor configuration;
- the trends on operating conditions that support a decrease on the maximum surface temperature in the non-adiabatic reactor were also responsible for a continuous deviation of the monolith outlet temperature from the adiabatic value;
- radiative heat losses were responsible for a slightly selective exothermic reaction pathway verified for all fuels. As a consequence, a lower importance of endothermic reforming reactions was observed contributing to a low integral fuel conversion;
- integral fuel conversion, CO selectivity and reforming efficiency in the non-adiabatic reactor were always lower than in the adiabatic reactor configuration;
- H_2 selectivity attained in the non-adiabatic reactor for pure methane was lower for low air to fuel equivalence ratios and higher for high air to fuel equivalence ratios than that achieved in adiabatic conditions;
- H_2/CO ratio was always higher for non-adiabatic conditions;
- the qualitative response of temperature profiles, relative radiative heat losses and chemical heat release to variations on fuel flow rate were similar for the three fuel mixtures.

The non-adiabatic reactor configuration under certain operating conditions (low fuel flow rates, high air to fuel equivalence ratios and supplied by fuels of high power density) proved to allow a significant decrease of the maximum catalyst temperature comparing to the adiabatic reactor configuration. This is of particular importance to prevent catalyst deactivation in order to guarantee a catalyst long term operation.

Acknowledgments

The authors would like to thank the financial support received from the European Commission within the 7th framework program (CP-IP 260105 FC-DISTRICT).

REFERENCES

[1] Hickman DA, Schmidt LD. Synthesis gas formation by direct oxidation of methane over Pt monoliths. J Catal 1992;138:267–82.

[2] Hickman DA, Haupfear EA, Schmidt LD. Synthesis gas formation by direct oxidation of methane over Rh monoliths. Catal Lett 1993;17:223–37.
[3] Hickman DA, Schmidt LD. Steps in CH_4 oxidation on Pt and Rh surfaces: high-temperature reactor simulations. AIChE J 1993;39:1164–77.
[4] Hickman DA, Schmidt LD. Production of syngas by direct catalytic oxidation of methane. Science 1993;259:343–6.
[5] Groppi G, Beretta A, Tronconi E. Monolithic catalysis for gas-phase syntheses of chemicals. In: Cybulski A, Moulijn JA, editors. Structured catalysts and reactors. Boca Raton: CRC Press; 2006. p. 243–310.
[6] Neumann D, Kirchhoff M, Veser G. Towards an efficient process for small-scale, decentralized conversion of methane to synthesis gas: combined reactor engineering and catalyst synthesis. Catal Today 2004;98:565–74.
[7] Aicher T, Lenz B, Gschnell F, Groos U, Federici F, Caprile L, et al. Fuel processors for fuel cell APU applications. J Power Sources 2006;154:503–8.
[8] York APE, Xiao T, Green MLH. Brief overview of the partial oxidation of methane to synthesis gas. Top Catal 2003;22:345–58.
[9] Schwiedernoch R, Tischer S, Correa C, Deutschmann O. Experimental and numerical study on the transient behavior of partial oxidation of methane in a catalytic monolith. Chem Eng Sci 2003;58:633–42.
[10] Mhadeshwar AB, Vlachos DG. Hierarchical multiscale mechanism development for methane partial oxidation and reforming and for thermal decomposition of oxygenates on Rh. J Phys Chem B 2005;109:16819–35.
[11] Maestri M, Vlachos DG, Beretta A, Groppi G, Tronconi E. A C_1 microkinetic model for methane conversion to syngas on Rh/Al_2O_3. AIChE J 2009;55:993–1008.
[12] Tavazzi I, Beretta A, Groppi G, Forzatti P. An investigation of methane partial oxidation kinetics over Rh-supported catalysts. Stud Surf Sci Catal 2004;147:163–8.
[13] Maestri M, Beretta A, Groppi G, Tronconi E, Forzatti P. Comparison among structured and packed-bed reactors for the catalytic partial oxidation of CH_4 at short contact times. Catal Today 2005;105:709–17.
[14] Donazzi A, Beretta A, Groppi G, Forzatti P. Catalytic partial oxidation of methane over a 4% $Rh/\alpha\text{-}Al_2O_3$ catalyst. Part I: kinetic study in annular reactor. J Catal 2008;255:241–58.
[15] Hartmann M, Maier L, Minh HD, Deutschmann O. Catalytic partial oxidation of iso-octane over rhodium catalysts: an experimental, modeling, and simulation study. Combust Flame 2010;157:1771–82.
[16] Maier L, Hartmann M, Tischer S, Deutschmann O. Interaction of heterogeneous and homogeneous kinetics with mass and heat transfer in catalytic reforming of logistic fuels. Combust Flame 2011;158:796–808.
[17] Hartmann M, Maier L, Deutschmann O. Hydrogen production by catalytic partial oxidation of iso-octane at varying flow rate and fuel/oxygen ratio: from detailed kinetics to reactor behavior. Appl Catal A Gen 2011;391:144–52.
[18] Kaltschmitt T, Diehm C, Deutschmann O. Catalytic partial oxidation of isooctane to hydrogen on rhodium catalysts: effect of tail-gas recycling. Ind Eng Chem Res 2012;51:7536–46.
[19] Livio D, Donazzi A, Beretta A, Groppi G, Forzatti P. Experimental and modeling analysis of the thermal behavior of an autothermal C_3H_8 catalytic partial oxidation reformer. Ind Eng Chem Res 2012;51:7573–83.
[20] Seyed-Reihani SA, Jackson GS. Influence of thermal conditions on partial oxidation of n-butane over supported Rh catalysts. Appl Catal A Gen 2009;353:181–92.
[21] Von Rickenbach J, Nabavi M, Zinovik I, Hotz N, Poulikakos D. A detailed surface reaction model for syngas production from butane over rhodium catalyst. Int J Hydrogen Energy 2011;36:12238–48.
[22] De Groote AM, Froment GF. Simulation of the catalytic partial oxidation of methane to synthesis gas. Appl Catal A Gen 1996;138:245–64.
[23] De Smet CRH, De Croon MHJM, Berger RJ, Marin GB, Schouten JC. Design of adiabatic fixed-bed reactors for the partial oxidation of methane to synthesis gas. Application to production of methanol and hydrogen-for-fuel-cells. Chem Eng Sci 2001;56:4849–61.
[24] Bizzi M, Basini L, Saracco G, Specchia V. Modeling a transport phenomena limited reactivity in short contact time catalytic partial oxidation reactors. Ind Eng Chem Res 2003;42:62–71.
[25] Tavazzi I, Maestri M, Beretta A, Groppi G, Tronconi E, Forzatti P. Steady-state and transient analysis of a CH_4-catalytic partial oxidation reformer. AIChE J 2006;52:3234–45.
[26] Dalle Nogare D, Degenstein NJ, Horn R, Canu P, Schmidt LD. Modeling spatially resolved profiles of methane partial oxidation on a Rh foam catalyst with detailed chemistry. J Catal 2008;258:131–42.
[27] Halabi MH, De Croon MHJM, Van der Schaaf J, Cobden PD, Schouten JC. Modeling and analysis of autothermal reforming of methane to hydrogen in a fixed bed reformer. Chem Eng J 2008;137:568–78.
[28] Beretta A, Groppi G, Lualdi M, Tavazzi I, Forzatti P. Experimental and modeling analysis of methane partial oxidation: transient and steady-state behavior of Rh-coated honeycomb monoliths. Ind Eng Chem Res 2009;48:3825–36.
[29] Donazzi A, Maestri M, Michael BC, Beretta A, Forzatti P, Groppi G, et al. Microkinetic modeling of spatially resolved autothermal CH_4 catalytic partial oxidation experiments over Rh-coated foams. J Catal 2010;275:270–9.
[30] Scognamiglio D, Russo L, Maffettone PL, Salemme L, Simeone M, Crescitelli S. Modelling and simulation of a catalytic autothermal methane reformer with Rh catalyst. Int J Hydrogen Energy 2012;37:263–75.
[31] Liu T, Snyder C, Veser G. Catalytic partial oxidation of methane: is a distinction between direct and indirect pathways meaningful? Ind Eng Chem Res 2007;46:9045–52.
[32] Ramaswamy RC, Ramachandran PA, Dudukovic MP. Modeling catalytic partial oxidation of methane to syngas in short-contact-time packed-bed reactors. Ind Eng Chem Res 2007;46:8638–51.
[33] Michael BC, Donazzi A, Schmidt LD. Effects of H_2O and CO_2 addition in catalytic partial oxidation of methane on Rh. J Catal 2009;265:117–29.
[34] Donazzi A, Maestri M, Beretta A, Groppi G, Tronconi E, Forzatti P. Microkinetic analysis of CH_4 CPO tests with CO_2-diluted feed streams. Appl Catal A Gen 2011;391:350–9.
[35] Froment GF, Bischoff KB. Chemical reactor analysis and design. New York: Wiley; 1990.
[36] Bodke AS, Bharadwaj SS, Schmidt LD. The effect of ceramic supports on partial oxidation of hydrocarbons over noble metal coated monoliths. J Catal 1998;179:138–49.
[37] Lee ST, Aris R. On the effects of radiative heat transfer in monoliths. Chem Eng Sci 1977;32:827–37.
[38] Boehman AL. Radiation heat transfer in catalytic monoliths. AIChE J 1998;44:2745–55.
[39] Karagiannidis S, Mantzaras J, Jackson G, Boulouchos K. Hetero-/homogeneous combustion and stability maps in methane-fueled catalytic microreactors. Proc Combust Inst 2007;31:3309–17.
[40] Kolaczkowski ST, Worth DJ. Modelling channel interactions in a non-adiabatic multichannel catalytic combustion reactor. Catal Today 1995;26:275–82.
[41] Modest MF. Radiative heat transfer. New York: McGraw-Hill; 1993.

[42] Mazumder S, Grimm M. Numerical investigation of radiation effects in monolithic catalytic combustion reactors. Int J Chem React Eng 2011:9.
[43] Beretta A, Donazzi A, Livio D, Maestri M, Groppi G, Tronconi E, et al. Optimal design of a CH_4 CPO-reformer with honeycomb catalyst: combined effect of catalyst load and channel size on the surface temperature profile. Catal Today 2011;171:79–83.
[44] Livio D, Donazzi A, Beretta A, Groppi G, Forzatti P. Optimal design of a CPO-reformer of light hydrocarbons with honeycomb catalyst: effect of frontal heat dispersions on the temperature profiles. Top Catal 2011;54:866–72.
[45] Kee RJ, Dixon-Lewis G, Warnatz J, Coltrin ME, Miller JA. A Fortran computer code package for the evaluation of gas-phase multicomponent transport properties. Tech. Rep. SAND86-8246. Sandia National Laboratories; 1986.
[46] Poinsot T, Veynante D. Theoretical and numerical combustion. Philadelphia, USA: R T Edwards; 2005.
[47] Veser G, Frauhammer J. Modelling steady state and ignition during catalytic methane oxidation in a monolith reactor. Chem Eng Sci 2000;55:2271–86.
[48] Shah RK, London AL. Laminar flow forced convection in ducts. New York: Academic Press; 1978.
[49] Wakao N, Smith JM. Diffusion in catalyst pellets. Chem Eng Sci 1962;17:825–34.
[50] Fuller EN, Schettler PD, Giddings JC. New method for prediction of binary gas-phase diffusion coefficients. Ind Eng Chem 1966;58:18–27.
[51] Siegel R, Howell JR. Thermal radiation heat transfer. Hemisphere Publishing Corporation; 1992.
[52] Karagiannidis S. Catalytic microreactors for portable power generation. Berlin: Springer; 2011.
[53] Karagiannidis S, Mantzaras J. Numerical investigation on the start-up of methane-fueled catalytic microreactors. Combust Flame 2010;157:1400–13.
[54] Noble JJ. The zone method: explicit matrix relations for total exchange areas. Int J Heat Mass Transfer 1975;18:261–9.
[55] Hayes RE, Kolaczkowski ST. Introduction to catalytic combustion. Amsterdam: Gordon and Breach Science; 1997.
[56] Kee RJ, Grcar JF, Smooke MD, Miller JA. Premix: a Fortran program for modeling steady laminar one-dimensional premixed flames. Tech. Rep. SAND85-8240. Sandia National Laboratories; 1985.
[57] Kee RJ, Rubley FM, Meeks E. CHEMKIN-II: a Fortran chemical kinetic package for the analysis of gas-phase chemical kinetics. Tech. Rep. SAND89-8009. Sandia National Laboratories; 1989.
[58] Smith GP, Golden DM, Frenklach M, Moriarty NW, Eiteneer B, Goldenberg M, et al. GRI-Mech 3.0. http://www.me.berkeley.edu/gri_mech/.